Fracture Characteristics and Damage Evolution of Coating Systems Under Four-Point Bending

Haiyan Liu, Lihong Liang,* Yingbiao Wang, and Yueguang Wei*

LNM, Institute of Mechanics, Chinese Academy of Sciences, Beijing 100190, China

The fracture and damage behaviors of ceramic coating/alloy substrate systems under four-point bending were investigated using a scanning electron microscope to observe *in situ* tests. Both the thin and thick coatings fractured by tensile instability at the pure bending sections, and multiple transverse cracks that were vertical to the interface occurred in the coatings. The average crack spacing was greater for the thick coatings than for the thin ones. A catastrophic failure model was developed to explain the damage evolution behavior of the coatings. The damage was found to increase sharply near the failure point.

Introduction

Thermal barrier coatings (TBC) with low thermal conductivity provide excellent thermal protection and wear resistance, and have been widely used in aircraft and blades of gas turbines to protect alloy substrates from the high-temperature environment.[1–6] Under service conditions, once spallation of the TBC occurs, the substrate becomes exposed to the high-temperature environment, and operation becomes impossible. Therefore, investigating the fracture mechanism and damage evolution behavior of TBC systems (or environmental barrier coatings and other coating systems) is important. Recent studies have shown that the typical failure modes of TBC or other coating systems include transverse cracking (perpendicular to the interface) in the ceramic top coat and delamination of the interface between the top coat and bond coat or between the bond coat and substrate after mechanical (i.e., tension and bending)[7–15] and thermal loadings.[16–20] The fracture modes are usually not independent of each other. In particular, delamination of the interface due to a mismatch of mechanical and thermal properties greatly affects the lifetime of a TBC system. The mechanism of interface delamination of thermal barrier coatings,[21] and the cracking mode and influence factors have been modeled based on the energy release rate.[22] A numerical lifetime model on durability of thermal barrier coatings was developed based on the fracture mechanical analysis and stress evolution calculation.[23]

Some researchers have studied the failure mechanism of TBC systems through tension,[7] three-point bending,[8–10] four-point bending tests,[11–15] thermal shock,[16,20] thermal

oxidation,[17] etc. For example, Chen *et al.* found that the bond coat processing method affects the interface delamination position.[7] Li *et al.* found two failure modes of TBC systems after three-point bending tests: thin coating systems are mainly dominated by transverse cracking in the ceramic coats, and thick coating systems are mainly dominated by the interface delamination between the coat and substrate.[10] Zhou *et al.* studied the crack propagation process of TBC systems during four-point bending tests.[14] However, the effect of the coating thickness on the fracture modes of a TBC system after a four-point bending test has not been reported. In fact, the failure modes of the TBC systems depend on many factors, such as the processing method, coating thickness, and loading and heat treatment conditions.

Some researchers have also studied the damage evolution of TBC systems in detail in tension or bending tests.[14,24–26] Qian *et al.* studied the damage evolution behavior of sandwiched TBC specimens during the tension test and proposed a damage mode involving the initiation, multiplication, and saturation of transverse cracks with the applied strain.[24] Mao *et al.* studied the crack propagation of the TBC under high-temperature tensile conditions;[25] they observed the change in the number of transverse cracks with the tensile strain and found a damage evolution rule similar to that previously reported.[14,24] Appleby *et al.* also studied real-time damage evaluations of environment barrier coatings under thermal–mechanical loading.[26] Saucedo-Mora *et al.* developed a multiscale finite element model to describe damage evolution in a thermal barrier coating.[27] Although the crack evolution has been studied statistically, a quantitative damage model of TBC systems is desired. Recently, a brittle damage model to describe the damage evolution behavior of TBC systems under three-

*lianglh@lnm.imech.ac.cn; ywei@lnm.imech.ac.cn

point bending was developed,[28] and TBC systems with different coating thicknesses and microstructures were found to obey the same power law as the catastrophic failure characteristics of the bulk brittle materials.[29–31] There is still a question regarding the damage rule for TBC systems under four-point bending in a pure bending case. Therefore, determining the dependence of the damage rule on the loading condition and stress state is important.

In this study, *in situ* four-point bending tests were performed and observed with a scanning electron microscope (SEM) to determine the fracture and damage evolution behavior of two kinds of TBC systems with different coating thicknesses in the pure bending sections. The thickness-dependent fracture characteristics were studied by observing the crack propagation and average crack spacing. The damage evolution behavior of the coatings was studied by observing the transverse crack evolution with the applied tensile stress, and the experimental results were compared with the catastrophic failure model to discover the damage rule.

Experimental Procedure

Well-polished and sand-blasted Ni-based super alloys with a thickness of 1.2 mm were used as the substrate materials. The thickness of the substrate was uniform for different TBC systems. NiCrAlY alloys were deposited on the substrates by air plasma spraying to form the bond coats with a thickness of approximate 10 μm. Then, 8 wt% Y_2O_3-stabilized ZrO_2 ceramics (YSZ) were deposited on the NiCrAlY alloys by air plasma spraying to form the ceramic top coats. The detailed preparation process is given in our previous work.[32–34] Two kinds of coatings with thicknesses of about 100 and 400 μm were prepared. Figure 1 shows the dimensions of the specimens. The length of the samples was 30 mm. The distance between the support and loading points is denoted by l, and the length of the pure bending section is denoted by l_0; both l and l_0 were

8 mm in this experiment. The thickness of the coatings (including the top and bond coats), thickness of the substrate, and width of the specimens are represented by h_c, h_s, and b, respectively; h_s is 1.2 mm. Table I lists the coating thicknesses and widths of the specimens. ξ is the distance between the interface and neutral plane of the systems.

In situ four-point bending tests were performed at room temperature and a constant loading rate of 0.1 mm/min. The load and displacement were controlled by the testing machine (Gatan Microtest 2000; Gatan, Pleasanton, CA). The load was applied to the bottom surface of the alloy substrates so that the coatings were in the tensile stress state. Figure 2 shows the polished section of a representative specimen. The TBC system is clearly a laminated structure with many pores and microcracks distributed randomly in the top and bond coats. The crack behavior of the specimens in the polished sections was observed in real time with the SEM. The experiment was interrupted at a series of different loading levels to take photos of the whole pure bending section of the specimens. The load–displacement curves and corresponding crack evolution micrographs were obtained simultaneously. The fracture characteristics and damage evolution behaviors of the two kinds of coating systems were compared.

Table I. Coating Thicknesses, Widths, Critical Loads, Fracture Strengths, and Average Crack Spacing of Two Kinds of Specimens

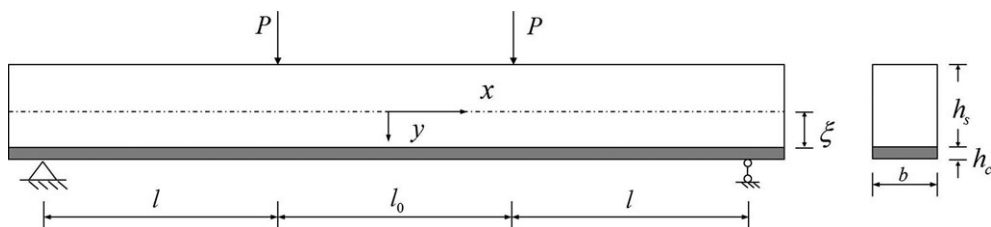| Sample symbol	h_c (μm)	b (μm)	P_c (N)	σ_{cr} (MPa)	d (mm)
S1	100	2430	93	129.6	0.23
S2	105	2500	92	125.3	0.22
S3	110	2400	94	134.1	0.24
S4	370	2800	105	155.9	0.89
S5	420	3000	98	138.8	0.80
S6	380	2900	96	138.3	0.80

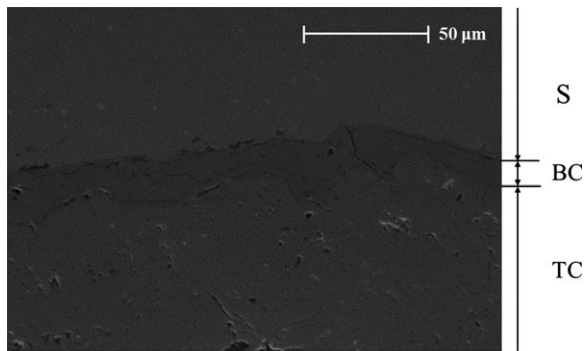*Fig. 1. Schematic shape and size of the four-point bending specimens.*

Fig. 2. Cross-sectional microstructure of the TBC system according to the SEM. S, substrate; BC, bond coat; TC, top coat.

Experimental Results

Figure 3 shows the measured load–displacement curve for the specimen with a coating thickness of 370 μm. The curve clearly shows a linear response up to the applied load of 105 N. The curve then shows nonlinear behavior due to the plastic deformation of the substrate and cracking in the transverse and interfacial directions of the TBC system. The small fluctuations in the curve correspond to the loading points at which the test was interrupted to take photographs. As each photograph was taken, the load dropped slightly without the change in displacement. The load was resumed and applied continuously after the photograph was taken.

Figure 4 shows the corresponding fracture micrographs of the left part of the pure bending section of the specimen at four loading levels in the four-point bending test. Pictures of the cracks in the same visual field are presented for better observation of the crack evolution. The right side figures show the enlargement of some cracks for clear observation of the morphologies. The whole fracture process can clearly be summarized as following four stages. With increasing load, the normal stress in the top coat reaches the tensile strength, which leads to the initiation of the transverse cracks in the top coat corresponding to point A on the curve in Fig. 3 (see Fig. 4a). The multiple transverse cracks rapidly proceed to saturation at load of 172 N, and the average crack spacing reaches 0.89 mm corresponding to point B on the curve in Fig. 3 (see Fig. 4b). After saturation, the cracks pass through the top coat/bond coat interface and propagate in the bond coat. When the transverse crack tips are close to the bond coat/substrate interface and the cracks deflect and propagate along this interface at the load of 189 N corresponding to point C on the curve in Fig. 3, these cracks are referred as local interface cracks (see Fig. 4c). Finally, some adjacent interface cracks link up, which results in local spallation of the coating when the load reaches 216 N corresponding to point D on the curve in Fig. 3 (see Fig. 4d). This phenomenon is similar to the results of previous reports.[10,14,24] Here, the four stages correspond to the initiation of the transverse cracks, saturation of these cracks, initiation of the local interface cracks, and occurrence of the local spallation. The first two stages are more important to evaluate the strength and damage failure rule of the coating systems. This is discussed in Theoretical Analysis.

Figure 5 shows the measured load–displacement curves for different specimens. The trends of the curves for specimens with almost the same coating thickness were consistent with each other. However, the thin coating systems had a smaller load than the thick ones at the same displacement as well as a smaller slope of the linear section. The main reason is that the thick coating systems had a greater equivalent bending stiffness based on the bending theory for laminated beams. In addition, only local spallation of the coatings occurred, so the coatings could continue to bear the load.

Figure 6 shows the fracture micrographs of the whole pure bending sections for S1 (i.e., thin coating sample) and S4 (i.e., thick coating sample) at the final loading points in the four-point bending tests. To facilitate clearer visualization, Fig. 7 also gives the side face and bottom surface micrographs for S1 and S5 (i.e., thick coating sample). The thin coating systems clearly had more transverse cracks, and the two kinds of coating systems both fractured by tensile instability at the pure bending sections. The main reason is that the pure bending sections had nearly no shear force; thus, it was not
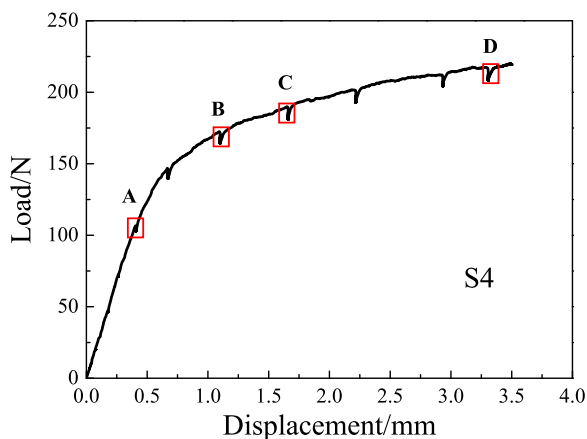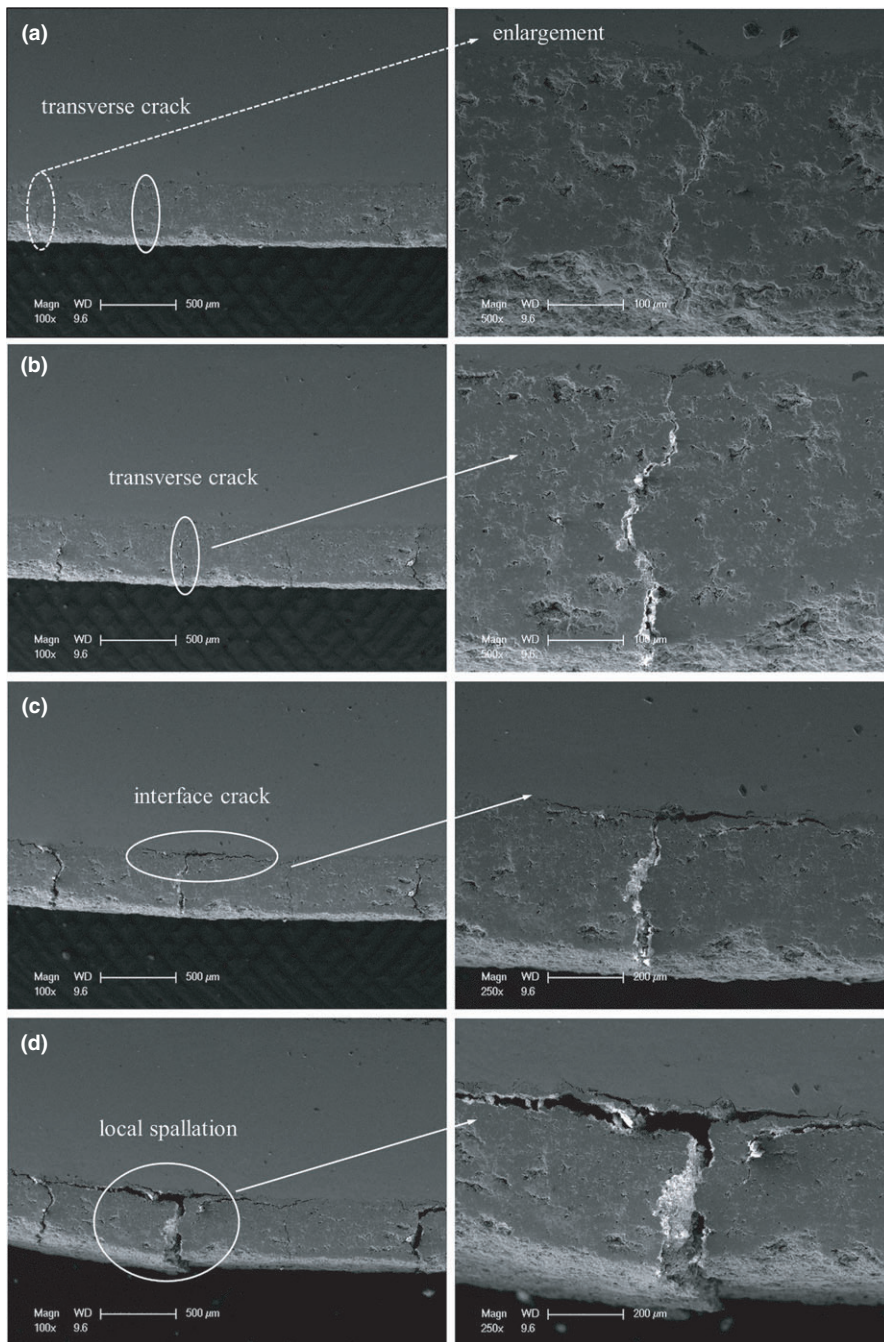

Fig. 3. Four-point bending load–displacement curve of sample S4. The rectangular frames denote the four crucial loading points (A–D). The corresponding morphologies are given in Figs. 4a–d.

Fig. 4. *In situ micrographs of the left part of the pure bending section of S4 at the loading levels of points A–D in Fig. 3: (a) the transverse cracks initiate in the top coat; (b) the multiple transverse cracks saturate; (c) the cracks propagate along the bond coat/substrate interface; (d) the adjacent interface cracks link up.*

easy for the main interface crack to emerge. When the normal stress in the top coats reached the tensile strength, the transverse cracks were initiated. Local decohesion for S1 was not apparent compared to S4. This may partly be because thin coating systems have a greater interface cohesive strength, so the interface is not easy to debond.

Figure 8a shows the load–displacement curve for sample S5, and Fig. 8b gives the fracture micrographs corresponding to the three points 1–3. The first two
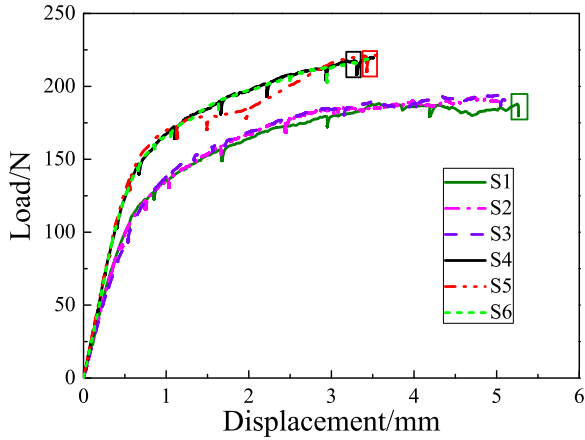
Fig. 5. Load–displacement curves of the thin coating specimens (S1–S3) and thick coating specimens (S4–S6). The rectangular frames denote the final loading levels, and the corresponding fracture micrographs are given in Figs. 6 and 7.
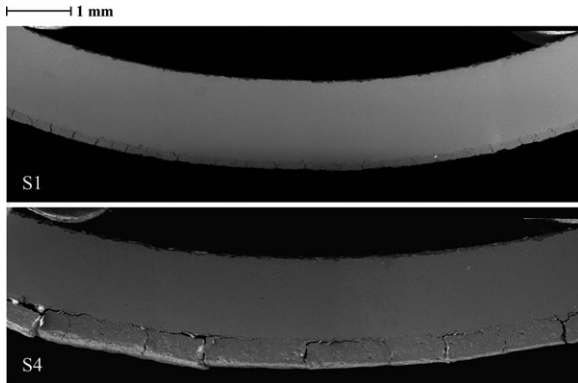

Fig. 6. Side view of the fracture morphologies of the whole pure bending sections of S1 and S4 at the final loading levels shown in Fig. 5.

stages of the whole fracture process were considered to predict the damage and failure in the tensile failure state. The crack pictures of the same visual field are presented for detailed observation of the damage evolution process. The crack micrographs were obtained in real time and it show the initiation, multiplication, and saturation of the transverse cracks, just like previous reports.[14,24,25] Note that Fig. 8b only shows the left part of the pure bending section owing to the limited visual field. Actually, many pictures with different visual fields covering the whole pure bending section corresponding to each point in the curve were taken. The length of the transverse cracks was measured by an image analysis method to consider the damage because coating systems subjected to the four-point bending test are dominated by tensile failure. The

calculation of the crack length corresponding to one loading point refers to all pictures covering the whole pure bending section.

In order to understand the thickness-dependent fracture characteristics and damage evolution behavior of the coatings with an applied stress, the bending theory for laminated beams was used to calculate the stress, the fracture energy rule was applied to explain the thickness-dependent crack spacing, and the catastrophic failure model was used to describe the damage evolution behavior and failure rule, as discussed in the next section.

Theoretical Analysis

The TBC system is simply treated as a two-layer beam comprising the coating and substrate, as shown in Fig. 1. According to the bending theory for laminated beams, the location of the neutral plane can be determined by $\xi = \frac{E_s h_s^2 - E_c h_c^2}{2(E_s h_s + E_c h_c)}$, and the curvature of the neutral plane can be determined by $\frac{1}{\rho} = \frac{M}{E_s I_s + E_c I_c} = \frac{M}{\overline{EI}}$. Here, E_s and E_c are the elastic moduli of the substrate and coating, respectively, and were measured to be $E_s = 200$ GPa and $E_c = 18$ GPa. $M = Pl$ is the bending moment of the pure bending section, and I_s and I_c are the moments of inertia of the substrate and coating, respectively. $\overline{EI} = E_s I_s + E_c I_c$ denotes the equivalent bending stiffness with $I_s = \int_{-h_s-\xi}^{\xi} by^2 \mathrm{d}y$ and $I_c = \int_{\xi}^{h_c+\xi} by^2 \mathrm{d}y$. With the tensile stress $\sigma = E\frac{y}{\rho}$, the normal stress at the midpoint of the beams at the coating edge can be obtained by

$$\sigma_c(y = h_c + \xi) =$$
$$\frac{3PlE_c}{b} \frac{E_c h_c^2 + 2E_s h_c h_s + E_s h_s^2}{0.5(E_s^2 h_s^4 + E_c^2 h_c^4) + 3E_c E_s h_c^2 h_s^2 + 2E_c E_s h_c h_s(h_c^2 + h_s^2)} \quad (1)$$

Let $c = \frac{E_c}{E_s}$, $\eta = \frac{h_c}{h_s}$. Then, Eq. (1) can be written in dimensionless form:

$$\frac{\sigma_c}{Pl/bh_s^2} = 3 \frac{c^2\eta^2 + c(1 + 2\eta)}{0.5(1 + c^2\eta^4) + 3c\eta^2 + 2c(\eta^3 + \eta)} \quad (2)$$

The load at the transition point from the linear to nonlinear response, which corresponds to the crack initiation of the TBC systems (see point A in Fig. 3), was taken as the critical load P_c to obtain the fracture strength σ_{cr} of the coatings based on Eq. (2). The ceramic coatings are inhomogeneous brittle materials, and defects including pores and microcracks are randomly distributed. Because the fracture behavior of the coatings is very sensitive to the defect distribution, the first
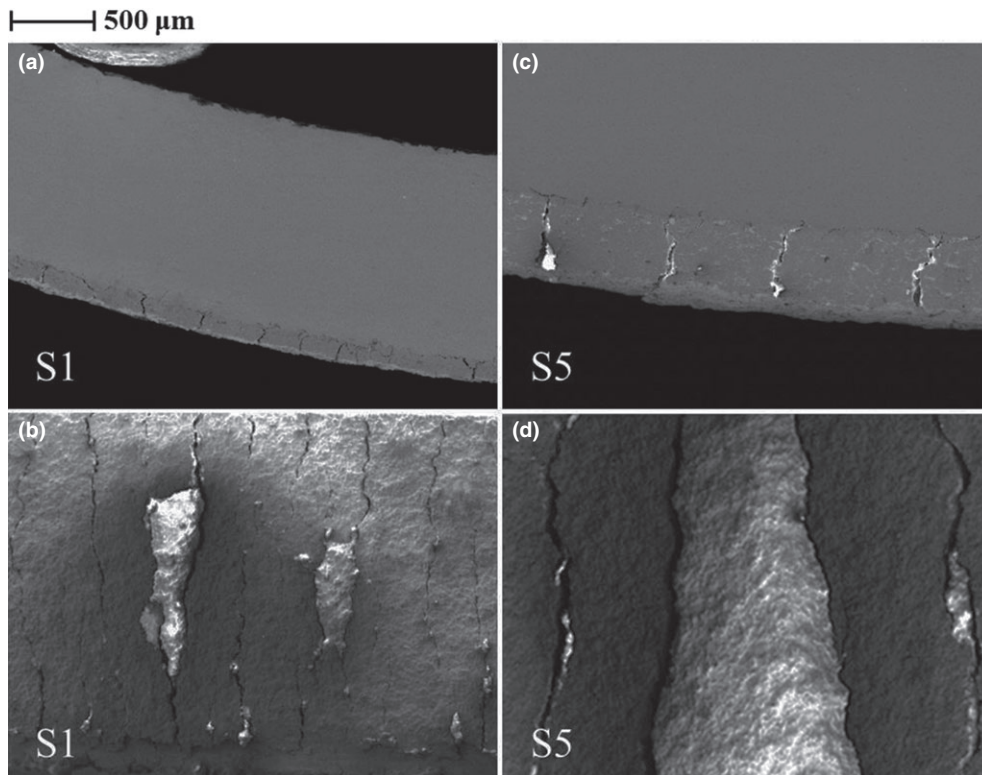
Fig. 7. Morphologies of the left parts of the pure bending sections of S1 and S5 at the final loading levels shown in Fig. 5: (a) side face of S1; (b) bottom surface of S1; (c) side face of S5; (d) bottom surface of S5.

transverse crack initiates at different loading levels for different specimens, which leads to a scattered distribution of the fracture strength. Table I presents the fracture strengths of the coatings, which were about 125.3–155.9 MPa. The thick coatings were stronger.

Table I indicates that the average crack spacing at the pure bending sections for the thick coatings (average: 0.86 mm) was greater than that for the thin coatings (average: 0.23 mm) according to the experimental results. According to the energy rule, the fracture energy of an elastic coating is equal to the surface energy of two newly formed surfaces. Thus, the fracture energy U of a coating can be calculated as

$$U = 2bh_cN\gamma \qquad (3)$$

where $N = \frac{l_0}{d}$ and N is the number of the transverse cracks. This can be counted based on the experiment micrographs. d and γ are the average crack spacing and surface energy density of the coatings, respectively. Equation (3) can be changed to

$$U = 2bl_0\gamma\frac{h_c}{d} \qquad (4)$$

Equations (3) and (4) indicate that the coating thickness is inversely proportional to the number of cracks and is proportional to the crack spacing when the fracture energy and specific surface energy as material constants and the other geometric parameters are fixed. This can provide a simple explanation for the fewer transverse cracks and larger crack spacing of the thick coating systems. Note that early cracks often initiate at some defects. The emergence of multiple transverse cracks is the main fracture mode, and tensile failure dominates the porous ceramic coatings at the pure bending sections. The transverse cracks saturate and propagate along the interface rapidly once the coating fractures. Therefore, the prestages of the local interface cracking should be considered to predict catastrophic failure.

Both kinds of coating systems fracture due to tensile instability at the pure bending sections, so the normalized transverse crack length is defined as the damage variable $D = \frac{L}{L_f}$. The normalized tensile stress $\lambda = \frac{\sigma}{\sigma_f}$ is taken as the controlling variable, L is the length of the transverse cracks, and the subscript f represents the failure point of the coating. The calculated crack length L corresponding to σ is the summed length of all
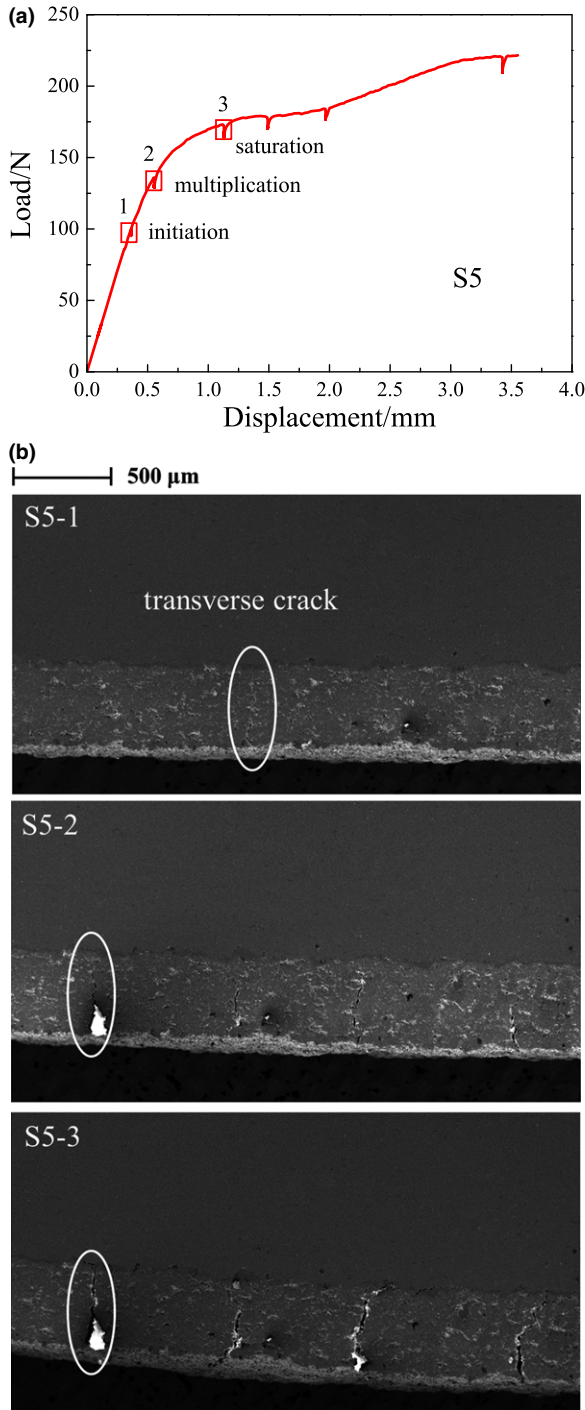
(a)

(b)

Fig. 8. (a) Load–displacement curve of the four-point bending test on S5 and (b) the transverse crack morphologies corresponding to points 1–3 in (a).

transverse cracks at the pure bending section. The failure crack length L_f and failure stress σ_f correspond to the point where the number of transverse cracks is saturated

at the end of the second stage of the whole fracture process (see point 3 in Fig. 8a). Then, the transverse cracks propagate along the interface, and the local interface cracks link up to lead to spallation of the coating. The components are then destroyed. The tensile stress σ is calculated according to Eq. (2).

The fracture of brittle materials induces catastrophic failure, so the damage rate tends to be infinite at the catastrophic point.[28–31] Then, we can obtain $\lim_{\lambda \to \lambda_f} = \frac{dD(\lambda)}{d\lambda} = \infty$ and $\lim_{D \to D_f} = \frac{d\lambda(D)}{dD} = 0$. If the controlling variable is continuous and derivative for the damage evolution of the system before catastrophic failure, we can use a Taylor expansion of the controlling variable at the catastrophic point to get

$$\lambda = \lambda_f + \lambda'(D_f) \times (D - D_f) + \frac{\lambda''(D_f)}{2} \times (D - D_f)^2 + o(D - D_f)^2$$

(5)

The damage variable D is calculated based on the crack length, as mentioned above. D_f represents the complete damage corresponding to λ_f, $D_f = 1$, and $\lambda_f = 1$ based on the above definition. $\lambda'(D_f)$ and $\lambda''(D_f)$ represent the first- and second-order derivations of the controlling variable at the failure point. By neglecting high-order terms (i.e., higher than second-order) and combining with $\lim_{D \to D_f} = \frac{d\lambda(D)}{dD} = 0$, Eq. (5) becomes

$$D = 1 - C(1 - \lambda)^{0.5}$$

(6)

where the damage coefficient is $C = \left[\frac{-\lambda''(D_f)}{2}\right]^{-0.5}$. Note that the initial damage $D_0 = \frac{L_0}{L_f}$ of one sample is determined by the initial crack length L_0, and the corresponding initial tensile stress is σ_0. The normalized initial controlling variable is $\lambda_0 = \frac{\sigma_0}{\sigma_f}$. By incorporating them into Eq. (6), we can acquire the damage coefficient $C = \frac{1 - D_0}{(1 - \lambda_0)^{0.5}}$. Therefore, the damage coefficient can be obtained as given in Table II based on experimental measurements. Equation (6) shows that the damage increases with stress and is completed when the stress

Table II. Normalized Initial Damage, Initial Stress, and Damage Coefficient Obtained From The Experimental Measurements of Two Kinds of Samples

	S1	S2	S3	S4	S5	S6
D_0	0.32	0.32	0.24	0.13	0.08	0.07
λ_0	0.66	0.57	0.59	0.61	0.51	0.60
C	1.18	1.04	1.19	1.40	1.33	1.48

reaches the failure point. The evolution of damage with the controlling variable obeys a power law relation with an exponent of 0.5.

The damage rate of the coating can be expressed by

$$R = \frac{dD}{d\lambda} = \frac{C}{2}(1 - \lambda)^{-0.5} \tag{7}$$

Equation (7) shows that the damage increases sharply near the catastrophic point, which agrees with the power law singularity of the damage rate with the controlling displacement based on experiments involving the catastrophic rupture of rocks.[31]

Figure 9 shows that the experimentally measured damage evolution (symbols) roughly corresponded with the power law function in Eq. (6) (curves) for the samples. The damage indicated a scattered distribution for different samples with almost the same coating thickness because the defects were randomly distributed in the brittle materials. The same results were indicated by the dispersed initial damage variables presented in Table II. In addition, the thick coating systems were damaged more quickly than the thin ones because the former (average: 1.39) had a greater damage coefficient C than the latter (average: 1.07). This is clearly indicated in Table II and agrees with the previous report on three-point bending.[28]

Figure 10 shows the damage rate versus the normalized tensile stress of the two kinds of coatings based on the experimental data and Eq. (7). The damage rate of the coatings tended to become infinite as the tensile stress neared the failure stress. Figure 11 shows the logarithmic relation of the damage rate versus the normalized tensile stress. The damage rate presented a scattered
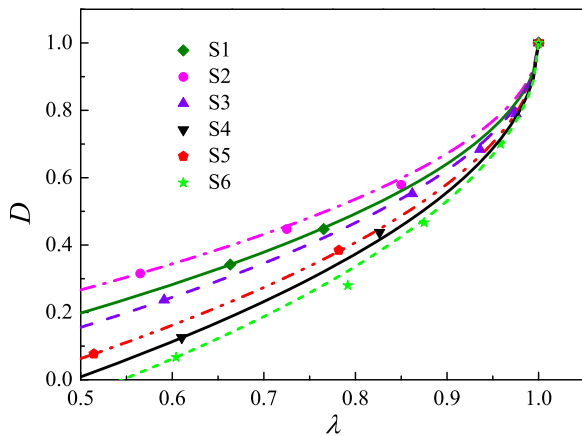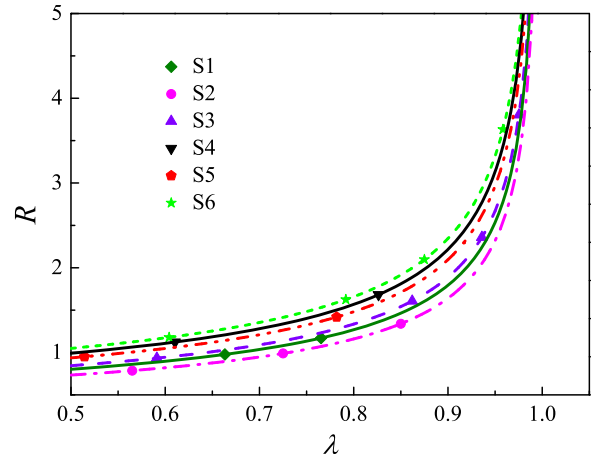

Fig. 10. Damage rate versus the normalized tensile stress of the two kinds of coating systems. The symbols are the experimental data, and the curves are based on Eq. (7).
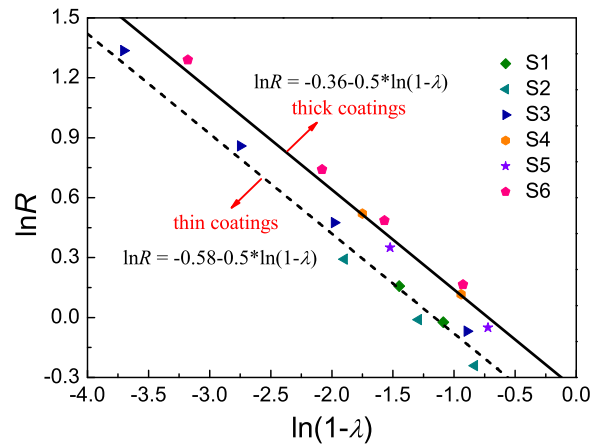

Fig. 11. Logarithmic relation of the damage rate versus the normalized tensile stress of the two kinds of coating systems. The symbols are the experimental data, and the curves, as denoted by the equations in the figure, are based on the average values of the corresponding samples.

Fig. 9. Damage variable versus the normalized tensile stress of the two kinds of coating systems. The symbols are the experimental data, and the curves are based on Eq. (6).

distribution for different samples. Furthermore, the slope of the curves was -0.5, which indicates the power law singularity of the damage rate. The intercept of the curves in Fig. 11 is equal to $\ln (C/2)$ in terms of Eq. (7). Thus, the intercepts was greater for the thick coatings than for the thin ones based on Table II. It is reasonable that the thick coating is damaged faster because it is closer to a bulk brittle material, and the catastrophic characteristics are more obvious. The damage coefficient was determined from the initial damage and the initial controlling variables. Based on the definition, the different values for the thick and thin coatings

may be related to the different residual stresses originating from the different thickness. The physical meaning of the damage coefficient will be further studied in the next work.

The experimental results obtained from the four-point bending tests agreed with the theoretical predictions (Figs. 9–11) based on the catastrophic failure model, similar to the three-point tests.[28] The difference in the two works was that the thick coatings were dominated by different stress failure modes, which led to different fracture characteristics. With the three-point bending tests,[28] shear failure of the interface dominated, and main interface delamination occurred for the thick coatings. With the four-point bending tests, however, tensile failure dominated, and multiple transverse cracks emerged in the pure bending case. Nevertheless, the damage rule was the same, and the damage evolution obeyed the power law relation with the same power exponent. The results of the present work validate the brittle damage catastrophic fracture model for coating systems regardless of the coating thickness, loading conditions, and stress state. Note that coats are usually used as high-temperature components, but the experiments here were carried out at room temperature based on the idea of equivalent thermal mismatch and mechanical energy (see Appendix). The thickness-dependent fracture behavior at room temperature is also important information and can provide a design guide for coatings. The fracture mode should help provide inspiration in studying high-temperature fracture mechanisms because *in situ* experiments at high temperature are difficult, and the mechanical parameters change at high temperature.

Conclusions

Experimental observation and theoretical analysis were performed to determine the fracture characteristics and damage evolution behavior of two kinds of TBC systems subjected to *in situ* four-point bending tests. The main conclusions can be summarized as follows:

1. The fracture process shows four stages with a continuously applied load: the transverse cracks first initiate and propagate in the top coat; they then multiply and become saturated; local interface cracks propagate between the bond coat and substrate; and finally, local spallation occurs when some adjacent interface cracks link up. The first two stages are important to evaluating the fracture strength and rule of damage evolution.
2. The fracture modes at the pure bending sections of the two kinds of coating systems are both dominated

by transverse cracks. The average crack spacing depends on the coating thickness, and the crack spacing is greater for thick coatings. Fracture energy analysis related to the surface energy explains the thickness-dependent fracture characteristics.
3. The catastrophic failure model effectively describes the damage evolution behavior of the coatings. The damage rate shows a power law singularity and the thick coating systems are damaged more quickly than the thin ones. The experimental results for the two kinds of coatings were all consistent with predictions based on the model.

Acknowledgments

Appendix

The Equivalent Thermal Mismatch and Mechanical Energy

According to the nonlinear delamination model of thin films, a thin isotropic film of thickness h_c bonded to a substrate is subject to a uniform stress σ_c as shown in Fig. 1a in Ref. 35. The stress state is similar to that under bending test in our work (the coating is in tension state). When the stored elastic energy per unit area in the film reaches the critical energy release rate $G_{crit}|_{Mechanics}$, delamination occurs as a interface crack. $G_{crit}|_{Mechanics}$ can be expressed by

$$G_{crit}|_{Mechanics} = \frac{1 - \upsilon_c^2}{2} \frac{\sigma_c^2 h_c}{E_c} \qquad (A1)$$

where E_c and υ_c are the Young's modulus and Poisson' ratio of the coating (i.e., the film), respectively.

Under thermal loading, the elastic energy per unit area in the coating due to thermal mismatch is $\frac{(1-\upsilon_c^2)}{2} E_c (\Delta\alpha \times \Delta T)^2 h_c$. When interface delamination occurs as a crack releasing the elastic energy, the critical energy release rate can be expressed by

$$G_{crit}|_{Temperature} = \frac{(1 - \upsilon_c^2)}{2} E_c (\Delta\alpha \times \Delta T)^2 h_c \qquad (A2)$$

where $\Delta\alpha = \alpha_s - \alpha_c$ denotes the difference of thermal expansion coefficients between the coating (α_c) and
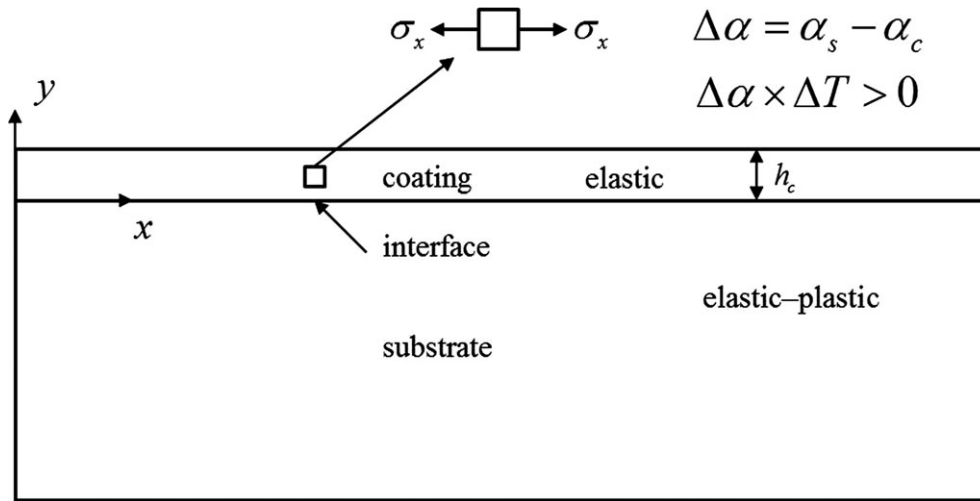
Fig. A1.   Thermal mismatch stress of elastic coating bonded on the substrate.

substrate (α_s), and ΔT denotes the temperature difference. The thermal stress state of the coating shown in Fig. A1 is also similar to the tensile stress state under bending test in our work.

Combining with Equations (A1) and (A2), according to the equivalent energy release rate, thermal and mechanical equivalent relation can be obtained as $(\Delta\alpha \times \Delta T)_c \sqrt{h_c}|_{\text{Temperature}} = \frac{\sigma_c}{E_c}\sqrt{h_c}|_{\text{Mechanics}}$. This means the corresponding thermal loading can cause equivalent stress σ_c, which can be expressed by

$$\sigma_c = E_c\Delta\alpha \times \Delta T \qquad (A3)$$

According to experimental results at room temperature, $\sigma_c = 160$ MPa, $E_c = 18$ GPa, $\alpha_s = 13.8 \times 10^{-6}$ K^{-1}, and $\alpha_c = 8 \times 10^{-6}$ K^{-1} are taken to calculate the temperature difference. The temperature difference is $\Delta T = 1533$ K neglecting changes of the thermal expansion coefficient and elastic modulus with temperature, i.e., when the temperature difference reaches 1533 K, the stress of 160 MPa is caused in the coating.

References

1. R. A. Miller, *J. Am. Ceram. Soc.*, 67 517–521 (1984).
2. B. A. Pint, I. G. Wright, W. Y. Lee, Y. Zhang, K. Prüßner, and K. B. Alexander, *Mater. Sci. Eng., A*, 245 201–211 (1998).
3. A. Kobayashi and T. Kitamura, *Vacuum*, 59 194–202 (2000).
4. A. G. Evans, D. R. Mumm, J. W. Hutchinson, G. H. Meier, and F. S. Pettit, *Prog. Mater Sci.*, 46 505–553 (2001).
5. N. P. Padture, M. Gell, and E. H. Jordan, *Science*, 296 280–284 (2002).
6. J. Wu, H. B. Guo, Y. Z. Gao, and S. K. Gong, *J. Eur. Ceram. Soc.*, 3 1881–1888 (2011).
7. Z. B. Chen, Z. G. Wang, and S. J. Zhu, *Surf. Coat. Technol.*, 205 3931–3938 (2011).
8. H. X. Deng, H. J. Shi, and S. Tsuruoka, *Surf. Coat. Technol.*, 204 3927–3934 (2010).
9. L. Yang, Z. C. Zhong, J. You, Q. M. Zhang, Y. C. Zhou, and W. Z. Tang, *Surf. Coat. Technol.*, 232 710–718 (2013).
10. X. N. Li, L. H. Liang, J. J. Xie, L. Chen, and Y. G. Wei, *Surf. Coat. Technol.*, 258 1039–1047 (2014).
11. I. Hofinger, M. Oechsner, H. Bahr, and M. V. Swain, *Int. J. Fract.*, 92 213–220 (1998).
12. A. K. Ray, N. Roy, and K. M. Godiwalla, *Bull. Mater. Sci.*, 24 203–209 (2001).
13. P. Y. Thery, M. Poulain, M. Dupeux, and M. Braccini, *J. Mater. Sci.*, 44 1726–1733 (2009).
14. Y. C. Zhou, T. Tonomori, A. Yoshida, L. Liu, G. Bignall, and T. Hashida, *Surf. Coat. Technol.*, 157 118–127 (2002).
15. M. Frommherz, A. Scholz, M. Oechsner, E. Bakan, and R. Vaßen, *Surf. Coat. Technol.*, 286 119–128 (2016).
16. B. Liang and C. X. Ding, *Surf. Coat. Technol.*, 197 185–192 (2005).
17. D. Renusch and M. Schütze, *Surf. Coat. Technol.*, 202 740–744 (2007).
18. M. Schweda, T. Beck, J. Malzbender, and L. Singheiser, *Surf. Coat. Technol.*, 276 368–373 (2015).
19. B. T. Richards, M. R. Begley, and H. N. G. Wadley, *J. Am. Ceram. Soc.*, 98 4066–4075 (2015).
20. Z. Fan, *et al.*, *Surf. Coat. Technol.*, 277 188–196 (2015).
21. R. Xu, X. Fan, and T. J. Wang, *Appl. Surf. Sci.*, 370 394–402 (2016).
22. J. Huang, B. C. Kim, S. Takayama, and M. D. Thouless, *J. Mater. Sci.*, 49 255–268 (2014).
23. C. Nordhorn, R. Mücke, D. E. Mack, and R. Vaßen, *Mech. Mater.*, 93 199–208 (2016).
24. L. H. Qian, S. J. Zhu, Y. Kagawa, and T. Kubo, *Surf. Coat. Technol.*, 173 178–184 (2003).
25. W. G. Mao, C. Y. Dai, L. Yang, and Y. C. Zhou, *Int. J. Fract.*, 151 107–120 (2008).
26. M. P. Appleby, D. Zhu, and G. N. Morscher, *Surf. Coat. Technol.*, 284 318–326 (2015).
27. L. Saucedo-Mora, K. Slámecka, U. Thandvamoorthy, and T. Z. Marrow, *Surf. Coat. Technol.*, 276 399–407 (2015).
28. L. H. Liang, X. N. Li, H. Y. Liu, Y. B. Wang, and Y. G. Wei, *Surf. Coat. Technol.*, 285 113–119 (2016).
29. Y. L. Bai, J. Bai, H. L. Li, F. J. Ke, and M. F. Xia, *Int. J. Impact Eng*, 24 685–701 (2000).
30. H. Y. Wang, Y. L. Bai, M. F. Xia, and F. J. Ke, *Mech. Mater.*, 38 57–67 (2006).
31. S. W. Hao, *et al.*, *Int. J. Rock. Mech. Min. Sci.*, 60 253–262 (2013).
32. Z. Chen, R. W. Trice, M. Besser, X. Yang, and D. Sordelet, *J. Mater. Sci.*, 39 4171–4178 (2004).
33. L. H. Liang, H. Wei, X. N. Li, and Y. G. Wei, *Surf. Coat. Technol.*, 236 525–530 (2013).
34. Y. X. Zhao, *et al.*, *Surf. Coat. Technol.*, 249 48–55 (2014).
35. Y. G. Wei and J. W. Hutchinson, *J. Mech. Phys. Solids*, 45 1137–1159 (1997).